Sustainable Materials and Technologies 40 (2024) e00901

Contents lists available at ScienceDirect

Sustainable Materials and Technologies

journal homepage: www.elsevier.com/locate/susmat

Ir metal nanoparticles and IrO_2 for acidic oxygen evolution reaction: Insight from Raman spectroscopy

Leonard Moriau [a,b], Mohammed Azeezulla Nazrulla [a,c], Anja Logar [a], Luka Pavko [a], Marjan Bele [a], Nejc Hodnik [a], Angelja Kjara Surca [a,*]

[a] National Institute of Chemistry, Hajdrihova 19, 1000 Ljubljana, Slovenia
[b] Centre of Excellence for Low-Carbon Technologies, Hajdrihova 19, 1000 Ljubljana, Slovenia
[c] Department of Chemistry, Manipal Institute of Technology, Manipal Academy of Higher Education, Manipal, Karnataka, India

ARTICLE INFO

Keywords:
IrO_2
Iridium
OER activity
Raman
Electrocatalysis
DFT
Solvation effect

ABSTRACT

Due to their high activity and stability, Ir-based materials are state-of-the-art electrocatalysts for oxygen evolution reaction (OER) under acidic conditions. However, many factors such as the influence of the activation/conditioning protocol and the resulting oxidation state or the effect of electrolyte adsorption on activity are still debated or overlooked. Herein, Raman spectroscopy was performed on commercial Ir black and IrO_2 nanopowders to reveal differences in the samples after activation, as well as adsorption of perchlorates. Specifically, three different activation protocols were performed, 0.05 to 1.45 V_{RHE} (activated), 0.05 to 1.6 V_{RHE} (activated-long range (l.r.)), and 1.1 to 1.6 V_{RHE} (activated-short range (s.r.)), resulting in different OER activity as well as different Raman spectra. However, only Ir(IV) bands remain visible in the *ex situ* Raman experiments, which was not sufficient to reveal the hydrated phases in the iridium samples. Therefore, *mimicked in situ* experiments were performed, which allowed the observation of the hydrated phase, particularly for Ir black, but also showed adsorption of perchlorate anions. In addition, the influence of solvation on Raman band shifts is revealed - along with DFT calculations. Overall, this work paves the way for our future *in situ* Raman spectroscopy experiments with iridium-based electrocatalysts during activation and OER.

1. Introduction

The development of a sustainable society urges us to overcome environmental issues (global warming, fossil fuels, *etc.*). Due to the intrinsically intermittent availability of renewable energy sources (wind, solar, *etc.*), they need to be converted and stored for future use. This can be achieved by converting water into hydrogen and oxygen through water electrolysis in a proton exchange membrane water electrolyzer (PEMWE), while there is a surplus of electricity produced [1–4]. Later, the two gases can be recombined in a polymer electrolyte membrane fuel cell (PEMFC) to produce electricity. Among the reactions that occur, the oxygen evolution reaction (OER) in PEMWE is of the highest concern due to its slow kinetic, large overpotentials and harsh conditions (acidic environment, elevated temperatures and highly oxidative potential). Due to this, OER is considered the bottleneck of electrochemical water splitting [3]. All these mentioned limitations considerably influence the possible choices of materials that can be used in electrolyzers. The only active and stable electrocatalysts under these conditions are platinum group metal (PGM) oxides. Although the most active material for OER is ruthenium oxide, iridium oxides have the best tradeoff between activity and stability [5–11]. For this reason, a range of IrO_2 materials, from crystalline to amorphous, have been examined. Structurally rigid rutile IrO_2 is outperformed by IrO_2 with flexible structures, Ir-hydrous oxides and also amorphous IrO_2 material [6,12]. Unfortunately, according to the state-of-the-art development, high iridium price and its scarcity are important drawbacks for commercialization. A strategy to reduce Ir loading is also the use of supporting materials, however, supports usually lack a stable response at high voltages [7,13,14].

The described issues related to the development of both active and stable catalysts for OER conditions demand the use of all appropriate and accessible characterization techniques that could give more insight into the processes occurring on the electrode surface. In our previous studies [15–18], we have already applied various suitable techniques to study the applicability, structure, performance, stability and degradation of Ir-based catalysts and appropriate supports. For example,

* Corresponding author.
E-mail address: angelja.k.surca@ki.si (A.K. Surca).

https://doi.org/10.1016/j.susmat.2024.e00901
Received 13 December 2023; Received in revised form 27 February 2024; Accepted 12 March 2024
Available online 15 March 2024

identical location transmission electron microscopy (IL-TEM), extended X-ray absorption fine structure (EXAFS), electrochemical flow cell coupled to an inductively coupled mass spectrometer (EFC-ICP-MS), electrochemical mass spectrometry (EC-MS) and AC voltammetry *etc.* [19,20] Another option for researching the described materials is Raman spectroscopy.

Raman spectroscopy is a well-known technique that gives a specific vibrational fingerprint of a sample. Its widespread use was achieved after the invention of charge-coupled devices in the eighties, which enabled multi-channel detection and decreased measurement times [21]. Furthermore, this technique is highly sensitive to local environments, defects and impurities. It is mostly non-destructive to samples and enables insight into the microscopic structural effects of materials [22,23]. Although Raman measurement of various types of samples can be straightforward, detection of some may be challenging. Such examples are black samples, as for example in the case of powdered high surface area electrocatalysts, for which the recording conditions must be carefully determined in order to preserve the properties of samples during the measurement. Using the appropriate laser excitation wavelength is crucial, as is its power, with the goal of avoiding burning, fluorescence or eventual oxidation. In most such cases, exact spectral bands can be detected using lower laser power and by sacrificing the signal-to-noise ratio. The dispersion of catalyst nanoparticles on the surface of the support can also be an issue, *i.e.*, how to find the location where the oxidation of the catalyst occurs. Consequently, different authors use films and bulk plates instead to get more defined spectra [24–27]. Perhaps it is precisely for the reasons listed above that Raman spectroscopy has not been sufficiently utilized for studies of catalysts and supports. Especially, this observation applies to many catalytic materials regarding the possibility of their use as an integral part of spectroelectrochemical approaches, *i.e.* to follow processes on electrodes during their operation.

In the case of Ir- and IrO_2-based samples, reports can be found on the Raman spectra of as-synthesized catalysts on different substrates (carbon nanotubes [13], activated carbon [8], $TiON_x$ [15], Li-IrO_x [12], lanthanide-$Ir_{1-n}O_x(OH)_y$ [28]). Interestingly, the examination was sometimes performed only on the spectral region of the carbon support (G,D bands), forgetting to examine the spectral region of the IrO_2 bands [8,10]. When metallic Ir is used as a catalytically active material, the appearance of bands in the Raman spectra indicates the partial oxidation of the metal to IrO_2. Namely, metallic Ir does not experimentally have active Raman modes.

IrO_2 belongs to a family of rutile-type transition metal dioxide compounds. Its monocrystal gives the distinct bands at 752 (A_{1g}), 728 (B_{2g}) and 561 (E_g) depending on whether the measurements are made on (100) or (101) faces [29]. The appearance and the shape of these bands in the Raman spectra of the prepared catalysts allow conclusions to be drawn about their microstructure. The spectra of nanocrystalline powders [12,13,28,30] and films [22,31,32] consist of two broad bands, *i.e.*, the E_g band and the overlapped $A_{1g} + B_{2g}$ band. Their shifts and broadening were systematically studied for films revealing the increase in particle size with increasing deposition temperature [22,31]. In addition, DFT calculations were performed to gain molecular insights into the structure and activity of Ir-based electrocatalysts [4,9,33–37].

The attempts to obtain the Raman spectra of electrochemically cycled catalytic samples are even rarer. However, in the case of Ir-based catalysts, the Raman approach was performed on hydrated IrO_x films electrochemically produced either on Ir foil (*ex situ*) [25] or roughened Au (*in situ*) [24,26] to avoid adhesion problems of powders. Namely, the roughened Au surface generates the surface-enhanced Raman spectroscopic (SERS) effect. Since SERS is limited to certain metal electrodes and, in particular, since this substrate can contribute to either electrochemical or spectroscopic response, Saeed et al. [27] applied the so-called shell-isolated nanoparticle-enhanced Raman spectroscopy (SHINERS). In this technique, the enhancement of the scattering signal occurs due to nanoparticles that are encapsulated in an inert shell. All these works [24–27] were performed on films in aqueous electrolytes (Table 1). They range from acids (i.e, H_2SO_4) to bases (i.e, NaOH) and solutions of various salts ($NaClO_4$, Na_2CO_3) which blurs the comparison. Under such conditions, the Ir-based films occur in hydrated forms which impose a series of broad and poorly resolved bands in the *in situ* Raman spectra. These works desribe transitions from Ir^{3+} to Ir^{4+} and Ir^{5+}, which were mainly identified electrochemically [24,27].

In this study, we aim to perform spectroelectrochemical Raman measurements of as-deposited, differently activated and degraded states directly on electrocatalysts. The samples are drop-casted IrO_2 and Ir nanoparticles on glassy carbon electrodes (GCE). Herein, we describe the results of *ex situ* and *mimicked in situ* studies with the aim for paving the way towards the *in situ* approach in the future. The samples were activated and degraded in 0.1 M $HClO_4$ electrolyte. Several Raman measurements were performed at different locations of each sample state. Both commercial powders (IrO_2, Ir black) were also analyzed using X-ray diffraction (XRD), energy-dispersive X-ray spectroscopy (EDS), X-ray photoelectron spectroscopy (XPS) and Raman spectroscopy. DFT calculations were made to support the measured Raman shifts. XPS was also applied to investigate the changes of the drop-casted samples in as-deposited and activated states.

2. Experimental

2.1. Electrocatalyst preparation

Commercial Ir black and IrO_2 were provided by Alfa Aesar and used without further purification. The electrocatalyst ink was prepared by mixing 5 mg of powder in 1 mL of Milli Q water (18.2 MΩ cm). Afterwards, the ink was placed in an ultrasonic bath (Ikra 4) for 10 min to obtain a homogeneous dispersion. Then, 20 μL of the suspension was drop-casted on a rotating disc electrode, *i.e.* glassy carbon electrode (GCE, 0.196 cm^2) embedded in polytetrafluoroethylene (PTFE). This resulted in a total loading of 510.2 $\mu g/cm^2$. The higher load compared to the usual rotating disc electrode (RDE) measurement [38] was necessary to obtain an interpretable signal during Raman measurements. The drop-casted electrocatalysts were allowed to dry overnight and 5 μL of a Nafion/isopropanol (1:50 *v*/v) solution was drop-casted and allowed to dry before the electrochemical experiments, resulting in 53.57 $\mu g/cm^2$.

2.2. Instrumental

Scanning electron microscopy (SEM) and SEM with energy dispersive X-ray analysis (SEM/EDX) were carried out using a field emission SEM Zeiss Supra TM35 VP (Carl Zeiss AG, Oberkochen, Germany), equipped with an EDX spectrometer - silicon drift detector EDX UltimMax 100 (Oxford Instruments, Oxford, UK). The operating voltage was set to 7 kV for SEM and 20 kV for SEM/EDX.

X-ray diffraction (XRD) measurements were carried out with a high-resolution X-ray powder diffractometer PANalytical X'Pert PRO MPD (PANalytical B.V., Almelo, The Netherlands) with alpha1 configuration ($CuK_{\alpha 1}$ $\lambda = 1.5406$ Å radiation). Diffractograms were recorded with a step size of 0.034° and an integration time of 100 s in the 2θ range from 10 to 60° using a fully open scanning X'Celerator detector. Phases were identified using the X'Pert HighScore Plus programme and the International Centre for Diffraction Data (ICDD) PDF-4+ 2021 database [39].

X-ray photoelectron spectroscopy (XPS) was performed with the Versa probe 3 AD (Phi, Chanhassen, US) using a monochromatic Al K_α X-ray source. For each measurement, spectra were acquired on a 1 × 1 mm analysis spot size with charge neutralizer turned on. High-resolution (HR) spectra were measured at pass energy of 27 eV and step of 0.1 eV. At least 15 sweeps were performed. The energy scale of XPS spectra and possible charging effect were corrected using the C 1 s peak of carbon at a binding energy (BE) of 284.8 eV. After acquisition of the spectra, the data were processed with the Multipak 9.0 Software.

The electrolyte (0.1 M $HClO_4$) was prepared by mixing concentrated

Table 1
Measurement characteristics and bands reported in the literature for Raman spectroscopy of IrO_x films.

Film	Electrodeposited hydrated IrO_x	Electrodeposited hydrous IrO_x	Electrodeposited hydrous IrO_x	Electrodeposited IrO_x	Drop-casted IrO_2 / Ir black	
Reference	[24]	[25]	[26]	[27]	This work	
Technique	SERS	Raman	SERS	SHINERS	Raman	
Type	*In situ*	*Ex situ*	*In situ*	*In situ*	*Ex situ*	
Laser wavelength	647.1 nm	780 nm	785 nm	633 nm	532 nm	
Substrate	Roughned Au	Ir foil (0.05 mm thick)	Roughned Au	GCE [d]	GCE [d]	
Electrolyte	(1) 0.5 M H_2SO_4 (2) 0.3 M Na_2CO_3	0.5 M H_2SO_4	(1) 0.1 M NaOH (2) 0.5 M H_2SO_4 [c]	1 M $NaClO_4$	0.1 M $HClO_4$	
Potential [a]	(1) 0.8 *V vs.* SCE [b] (~1.07 *vs.* RHE) (2) 0 V *vs.* SCE (~0.27 V *vs.* RHE)	0.8 V *vs.* RHE	(1) 0.8 V *vs.* RHE	Overview of bands in potential region Ir(3+), Ir(4+)	OCP [e] after being activated	
					IrO_2	Ir black
Positions of bands obtained at potential [a] (cm^{-1})		278 (α)		262 (α)		
		348 (β)		357 (β)		
			476 (γ)		465	465 sh [f]
	500	493 (γ)		504 (γ)		488
			527 (δ)		557	552 sh
		602 (δ)		608 (δ)		602
	620				634	
			595 (ε)			
		678 (ε)				
		713 (ε)		719 (ε)	728	724 sh
	774			773 (ξ)	746	744

[a] Potential, at which the Raman bands in this table are collected.
[b] Saturated calomel electrode.
[c] In this reference, the *in situ* Raman spectra recorded in 0.5 M H_2SO_4 are shown in *Supporting information*.
[d] Glassy carbon electrode.
[e] Open circuir potential.
[f] sh means shoulder band.

$HClO_4$ (Suprapur 70%, Merck) with Milli-Q water. The electrochemical protocols were performed in a two-compartment cell with a three-electrode system controlled by a potentiostat (ECi-200, Nordic electrochemistry). The catalysts deposited on GCE were mounted on a CTV 101 rotator (Radiometer Analytical) as the working electrode. The reference and counter electrodes were Ag/AgCl (BaSi) and carbon rod, respectively. The reference was separated from the other electrodes and placed in the second compartment to avoid any potential contamination by Cl^- ions. The reference potential compared to the reversible hydrogen electrode (RHE) was determined prior to any experiment by using Pt mesh as a working electrode and measuring the OCP in a H_2-saturated electrolyte. Otherwise, the electrolyte was saturated with N_2 during all the experiments. Different activation protocols were investigated. Namely, 100 cycles at 300 mV/s and 1600 rpm were performed in various potential ranges, 0.05 to 1.45 V_{RHE}, 1.1 to 1.6 V_{RHE} and 0.05 to 1.6 V_{RHE} for activation, short-range activation and long-range activation, respectively. Every protocol was performed on multiple catalysts for reproducibility. Few samples were selected for Raman spectroscopy and were rinsed with water and dried. After recording the Raman spectra, accelerated degradation was performed by applying a constant current of 2 mA for 2 h at 3600 rpm. The other samples were employed to investigate the impact of activation protocols on the OER activity. After the activation protocol, the OER activity was measured by cycling 10 times between 1.2 and 1.6 V_{RHE} at 10 mV/s. The resistance was compensated by 95%. The activity measurements were performed on at least three different samples for each activation protocol.

The Raman spectra were measured on a WITec alpha 300 confocal Raman spectrometer using a green excitation laser light of 532 nm. The spectra of electrocatalyst powders (IrO_2 and Ir black) were recorded on a Si wafer substrate, using 20× objective, 100 scans, an integration time of 0.5 s and various laser powers (1 to 3.2 mW). The time-dependent spectra of Ir black powder were performed at the laser powers of 1, 1.2, 1.6 and 3.2 mW in order to determine its stability during 2 h exposure. In this case, the spectra were recorded at the same site.

Ex situ Raman spectra of drop-casted IrO_2 or Ir black on GCE were measured using 20× objective, 100 scans, an integration time of 0.5 s and a laser power of 1.6 mW. Prior to *ex situ* Raman measurements, the samples were electrochemically treated, gently rinsed with Milli-Q water, left to dry and then transferred under the objective of the Raman spectrometer. The drop-casted (as-deposited) samples were measured first, followed by the measurement of differently activated samples. Several electrodes (2–3) were prepared to examine each state. Three to eight measurements of spectra were performed at different locations on the sample. These spectra were then normalized to the most intense E_g band in the spectral range 500–800 cm^{-1} using OPUS 7.8 software program (Bruker Optik GmbH). The same program was used for the calculation of the average spectrum from the normalized spectra of each state.

Raman spectra of drop-casted GCE/IrO_2 or GCE/Ir black that were used in *mimicked in situ* experiment were recorded using 20× objective, 50 scans and the integration time of 4 s. The laser power was 0.7 or 1.1 mW. For these measurements, the activation was performed in the potential range from 0.05 to 1.45 V_{RHE}, with a scan rate of 500 mV/s and 500 cycles. Activation was finished at 0.05 V_{RHE} and the transfer of the electrode was made with a drop of electrolyte.

2.3. DFT calculations

Density functional theory (DFT) based calculations for all the aperiodic models of Ir black and IrO_2 were performed by employing Gaussian 16 (Revision C.02) suite of packages [40]. The long-range-corrected version of B3LYP using the Coulomb-attenuating method, CAM-B3LYP (Becke, three-parameter, Lee-Yang-Parr) exchange-correlation functional as well as just hybrid B3LYP (Becke, three-parameter, Lee-Yang-Parr) exchange-correlation functionals were used for comparison of Raman simulations in a model system representing

aperiodic Ir atomic cluster, Ir_{12} (as shown in Scheme A and, for IrO_2, in Scheme B in *Supplementary information*). This Ir cluster, for the partial oxidation of Ir black formed prior to water oxidation, Ir_{12} model system was functionalized with 1:1 -OH groups (represented as Ir_{12}-all-OH) (hydrous oxide). The quasi-relativistic effective core potentials (ECP) for all Ir atoms under study have been described with LANL2DZ. Moreover, Stuttgart-Dresden ECPs (SDD) have also been used to compare the simulation of Raman signatures in the model Ir_{12}. Dunning's correlation consistent basis sets with triple zeta valence polarization (cc-PVTZ) basis sets have been used for all the C, O, Cl and H atoms in all the aperiodic models as shown in *Section 3.1*.

All the calculations involve spin-polarized DFT, *i.e.* unrestricted Kohn-Sham formalism has been utilized for the ground state (GS) optimizations of all structures. Default convergence criterion with Berny algorithm and extra quadratically convergent (XQC) self-consistent field (SCF) method was used for all the GS geometry optimizations. Optimized geometries are confirmed as the local minima with all the positive vibrational frequencies from simulated infrared (IR) spectra. Grimme's DFT-D3 dispersion correction was also employed in all the calculations. Natural atomic orbital and natural bond orbital analysis (NBO) program of Gaussian NBO Version 3.1 [41] was used for the spin density mapping and orbital analysis wherever needed. All the images were plotted from Gauss View 5.0 and VESTA 3.4.4. [42] For the Ir_{12} singlet geometry was found to be the ground state structure compared to the triplet state with relative energy difference of 0.36 eV. Relative energy (Rel E, in eV) is calculated from the eq. 1.

$$Rel\ E = E_{GS} - E_{HES} \quad (1)$$

where E_{GS} corresponds to total energy of the lowest energy structures, and E_{HES} corresponds to total energy of the high energy structures, respectively.

The models drawn in *Section 3.1* are used to describe the bulk IrO_2 and cleaved surfaces with possible fully coordinated to under-coordinated Ir and also if the octahedral coordination of Ir is occupied by the H_2O molecule prior to water oxidation or OER relevant conditions. The solvent reaction field for all studied systems of Ir is modeled with Polarizable Continuum Model (PCM) using the conductor-like PCM (CPCM) formalism. As the OER relevant conditions include the aqueous medium, we used water as a solvent in CPCM calculations.

3. Results and discussion

3.1. Characterization of commercial IrO_2 and Ir black powders

Commercial IrO_2 and Ir black powders were examined using XRD and EDS analyses (Figs. 1, 2, Table 2). The XRD diffractograms reveal characteristic peaks of metallic Ir and rutile IrO_2. In the case of Ir black, sharp peaks with a broader base are observed at 40.7° and 47.3°, corresponding to (111) and (200) diffractions of Ir (PDF 04–001-0838). The shape of the two peaks indicates that the sample is generally composed of small Ir nanoparticles (broad base) with the presence of some larger particles (sharp peak). On the other hand, the IrO_2 spectrum presents characteristic peaks at 28.0°, 34.5°, 39.9°, 40.7° and 53.8°, as well as a double peak at 57.9° and 58.2° corresponding to (110), (101), (200), (111), (211), (220) and (002) planes of tetragonal IrO_2 (PDF 04–009-8479). Interestingly, the presence of very low-intensity peaks at 40.8° and 47.4° may indicate a small portion of metallic Ir in the sample, as already found by other authors [43]. However, the amount is negligible since only the latter diffraction may originate solely from metallic Ir. The former diffraction appears to overlap the position, at which the low-intensity diffraction of IrO_2 also occurs ($2\Theta = 40.7°$). Furthermore, the XPS measurement of IrO_2 powder confirmed the presence of Ir only in the 4+ oxidation state, as discussed in *Section 3.3*.

SEM images reveal quite a uniform layer of untreated Ir black powder at the 100 μm scale, however, further magnification shows

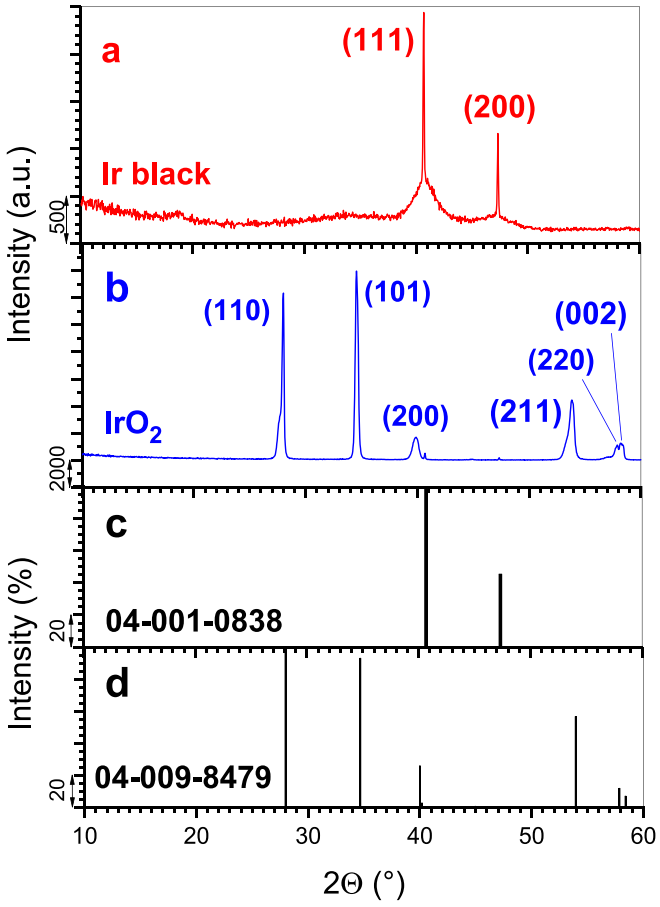

Fig. 1. XRD diffractograms of powders: a) Ir black and b) IrO_2. PDF patterns are shown for comparison: c) Ir, PDF 04–001-0838 and d) IrO_2, PDF 04–009-8479.

distinct differences between certain regions (Fig. 2A, Fig. S1 A in *Supplementary information*). Surprisingly, EDS spectra of Ir black obtained on larger areas reveal large amounts of oxygen in addition to Ir (Table 2). Specifically, spectra 1 and 2, recorded over a larger area, resulted in 55–57 at.% Ir and 43–45 at.% O, respectively. When recorded over a much smaller area (spectra 3, 4 in Fig. S1 A), the EDS measurement resulted in a much higher percentage of Ir (> 74 at.%). These measurements revealed the high affinity of Ir nanoparticles for oxygen *via* oxidation propensity of Ir nanoparticles, referred to as native oxide formation, or oxygen and oxygen-containing species adsorption. On the other hand, the EDS spectra of IrO_2 compound found the presence of about 41.6 at.% Ir and 58.4 at.% O (Fig. 2B, Fig. S1 B in *Supplementary information*). Ir in this compound is in excess relative to the compound formula, which can be explained by the presence of metallic Ir in the sample (visible from XRD in Fig. 1b). The particle size distribution of IrO_2 and Ir black was previously measured by TEM and were found to be similar, *e.g.* 9.8 nm for Ir black and 8.9 nm for IrO_2, respectively [16].

The Raman spectra of IrO_2 and Ir black powders reveal two bands at 548 and 719 cm^{-1} (Fig. 3). The former band corresponds to the E_g mode, while the latter to the overlapping vibrational modes B_{2g} and A_{1g}. These bands are red shifted relative to the E_g, B_{2g} and A_{1g} modes of the monocrystalline IrO_2 (561, 728 and 752 cm^{-1}) [29]. Such red shifts have already been reported for IrO_2 powders [12,13,28,30] and films [22,31,32,43], but the magnitude of the shifts varied. In case where the overlapping B_{2g} and A_{1g} bands are more discerned (films [22,31,43], IrO_2 nanocrystals on carbon nanotubes [13]), the bands are positioned closer to the modes of monocrystal, and A_{1g} is more intense compared to B_{2g}. In our spectra of IrO_2 and Ir black powders (Fig. 3), the overlapping band at 719 cm^{-1} reveals a red-frequency broadening that probably

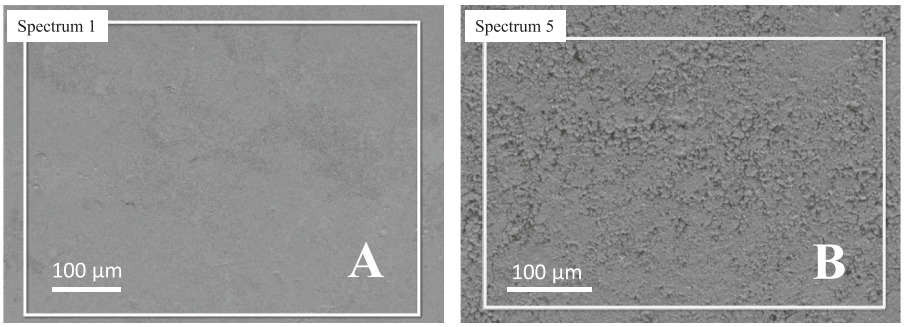

Fig. 2. SEM micrographs of: A) Ir black and B) IrO_2 with marked areas used for elemental determination by EDS.

Table 2
Elemental composition of IrO_2 and Ir black determined (in at.%) using EDS.

Compound	Spectrum	Ir	O
Ir black	1	55.5	44.5
	2	56.2	43.8
	3	76.0	24.0
	4	74.6	25.4
IrO_2	5	41.6	58.4

*Number of each spectrum measurement indicated by rectangles in Fig. 2 and Fig. S1 in *Supplementary Information.*

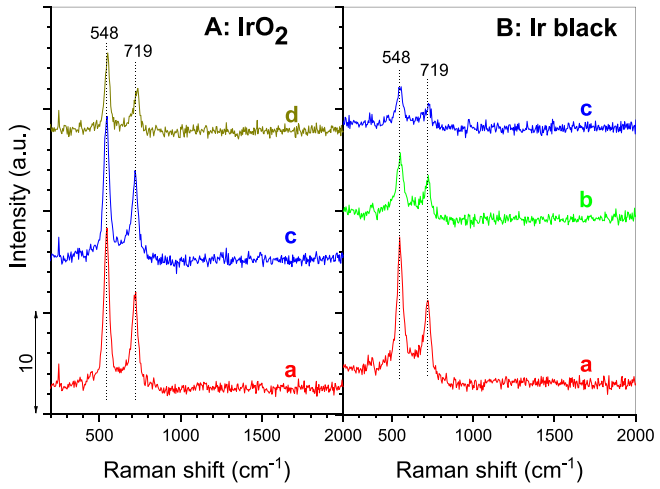

Fig. 3. Raman spectra of IrO_2 (A) and Ir black (B) powders on a silicon substrate. Laser powers used were: a) 1.6 mW, b) 1.2 mW, c) 1 mW and d) 0.7 mW.

originates comes from the B_{2g} mode; the A_{1g} mode is more intense. This broadening is more notable when the spectra were recorded at lower laser powers (Figure 3Ad, Bc).

The fact that the Raman spectra of IrO_2 and Ir black powders have bands at the same positions is consistent with the EDS analysis (Fig. 2, Table 2, Fig. S1 in *Supplementary information*). Although metallic Ir is Raman inactive, its partial oxidation in air gives rise to oxide spectra. XRD confirms the crystalline diffractions of IrO_2 commercial powder (Fig. 1b). However, for Ir black powder IrO_2 diffractions are not noted (Fig. 1a) which - in line with Raman spectra (Fig. 3B) and EDS - suggests the presence of an amorphous oxide and short-range ordering. The stability of the Raman signals obtained from the Ir black powder was also verified over a period of 2 h under four different laser powers (Fig. S2 in *Supplementary information*).

According to the above description, we also need to examine the as-deposited (initial) samples intended for *ex situ* Raman measurements (see *Section 3.3.*). These samples were prepared by drop-casting the suspensions of either IrO_2 or Ir black on GCE. Since D and G bands of GCE can appear in the spectra of drop-casted samples, the Raman spectra of GCE are shown in Fig. S3 in *Supplementary information*. On the other hand, the bands of Nafion used to consolidate both types of samples on GCE are not observed in the Raman spectra due to its low concentration. The spectrum of Nafion is shown in Fig. S4 in *Supplementary information*.

It is interesting to note that the spectra of drop-casted GCE/IrO_2 and GCE/Ir black differ (Fig. 4) in contrast to their similar spectra of powders (Fig. 3). The GCE/IrO_2 bands appeared at 557 (E_g), 728 (B_{2g}) and 746 (A_{1g}) (Fig. 4A), *i.e.*, positions that are close to the vibrational modes of the IrO_2 monocrystal [29]. When comparing the drop-casted GCE/IrO_2 sample (Fig. 4A) and the IrO_2 powder (Fig. 3A), E_g band shifted for 9 cm^{-1}. In addition, the overlapping $B_{2g} + A_{1g}$ band of the IrO_2 powder at 719 cm^{-1} (Fig. 3A) resolved into more distinct B_{2g} and A_{1g} modes for GCE/IrO_2 sample (Fig. 4A). In the case of GCE/Ir black sample (Fig. 4B), the bands have lower intensity due to a lower content of oxidized iridium and its amorphous nature (Table 2). Only two bands at 552 and 724 cm^{-1} can be observed (Fig. 4B), and they are shifted approximately 4–5 cm^{-1} relative to the Ir black powder (Fig. 3B). For ease of comparison, all shifts are collected in Fig. 4C. As discussed above, Raman shifts between powdered samples [12,13,28,30], films [22,31,32,43] and monocrystal [29] have already been noted, and ascribed to residual stress effects [13,32], particle size [13], microcrystallinity [22,31] and local disorder [22,31]. None of the studies mentioned the possibility of the tendency of oxide to orient when deposited on a surface, or a solvation effect that arises from the film preparations (from ultrasonication of suspensions, different electrolytes, *etc.*). Further experimental studies are aimed at elucidating these effects more clearly while at this point DFT calculations have been performed to gain more detailed insight into the molecular vibrations.

In order to discern the observed Raman shifts, we carried out DFT calculations with the aid of model systems. DFT-based calculations with aperiodic model systems are robust and inexpensive for structure-property calculations as well as offer a deeper understanding of the electronic structure of Ir-based nanoelectrocatalyts [25,26,44,45]. The basic aperiodic models for IrO_2 (as shown in Scheme B in *Supplementary information*) are chosen based on the works of Pavlović et al. [25,26] These aperiodic models are for both samples shown in Fig. 5. Specifically, we have built the aperiodic models with octahedral coordination of Ir with six -OH groups along with undercoordinated Ir with five -OH groups. Moreover, H_2O-occupied Ir with octahedral coordination has also been modeled to study the explicit and implicit solvation role. A comparison of the Raman signatures over all the various exchange-correlation functionals, as described in computational methodology, is tabulated in Table 3 for the aperiodic model $Ir(OH)_5$. The Raman shifts for all the signatures of IrO_2 calculated from LANL2DZ-UB3LYP are closest to the values reported by Huang et al. [29] and hence, for the rest of all the studied systems, this methodology has been employed to understand - as well as to substantiate - the measured Raman shifts.

Raman shifts for aperiodic nanostructured oxides and incipient hydrous oxide are tabulated in Table 4. The reported values in brackets

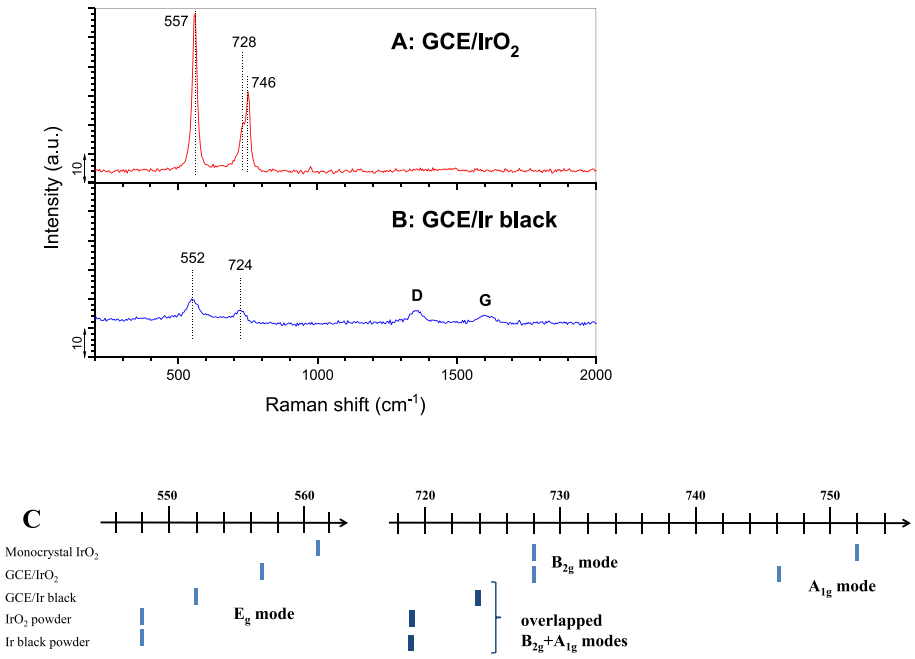

Fig. 4. Raman spectra of drop-casted samples on GCE: A) GCE/IrO_2 and B) GCE/Ir black. The laser power was 1.6 mW. C) Comparison of the Raman band positions of the investigated samples with regard to the reported modes of monocrystal [29]. D and G bands belong to the GCE electrode.

correspond to the implicit solvation model. Moreover, for all aperiodic models, the Raman shifts studied in CPCM solvation effect are all significantly (five to eight times) more intense. It is evident that the soft B_{1g} modes are of the lowest intensity and are rarely visible experimentally. Except for the highly symmetric $Ir(OH)_6$ octahedral geometry, all the simulated Raman active modes, with and without solvation effect, approach the values reported for monocrystalline IrO_2 [29] (Table 4), and the experimentally detected E_g, B_{2g} and A_{1g} bands in Figs. 3 and 4. Solvents are also known to affect vibrational (IR and Raman) spectra. The representative calculated vibrations are shown in Scheme C in *Supplementary Information*.

3.2. Electrochemical measurements

The activity of iridium towards OER strongly dependens on the chemical environment of the active site, *i.e.* its degree of oxidation. It has been shown that various synthesis processes [46], annealing temperatures [47,48] or activation protocols [49,50] can result in the creation of various active sites and thus different OER activity [51]. Herein, three activation protocols with different potential windows were performed (Table 5) and their influence on activity was investigated. The first protocol (activated) is close to what is often used in literature, *i.e.* fast cycling from a low potential of 0.05 V_{RHE} to a potential close to OER onset potential (1.45 V_{RHE}). This protocol is used to grow a thin hydrous oxide layer over metallic iridium (Ir black sample) by repeatedly cycling between the oxidizing and reducing potential [20,37,51–59]. In the case of IrO_2 sample, which is already oxidized, a thinner hydrous oxide is expected, and thus a lower activity [60–63].

The second protocol (activated – long range) extends the potential window to 1.6 V_{RHE} (cycling between 0.05 and 1.6 V_{RHE}) [37]. This is a more oxidative condition and thus an overall thicker oxide layer is expected, as the upper potential limit determines the growth and thickness of the oxide layer. It should positively influence the OER activity. However, under such conditions, the Ir surface may undergo structural (formation of surface defects, buckling and roughening of the crystalline surface) and chemical (surface oxidation and Ir dissolution) changes [37,60,61].

The last protocol (activated – short range) consists of cycling the catalysts under OER conditions, *i.e.*, between 1.1 and 1.6 V_{RHE} [64,65]. In this case, the potential is not low enough to efficiently reduce IrO_2 and thus no hydrous oxide is produced, and an overall lower activity is expected. Similarly, oxides formed on Ir black will not be consequently reduced and thus the formation of more active sites should be hindered, and lower activity is expected.

Figure 6 shows the activity of IrO_2 and Ir black after the different activation protocols. It is visible that the long-range activation has the best impact on activity for IrO_2 while the short-range activation resulted in the lowest activity (Fig. 6A). This goes along with the possible formation of hydrous oxide in the case of long-range activation but not for short-range one. On the other hand, for Ir black, both activation and long-range activation resulted in similar OER activity (Fig. 6B). This is probably because it is easier to produce hydrous oxides on the metallic iridium that is partly oxidized to amorphous IrO_2 than on a more rigid rutile-like (IrO_2) structure. Thus both potential ranges create a sufficiently thick hydrous oxide layer on Ir black already after 100 cycles. Oppositely, Ir black presented a lower OER activity after the short-range activation.

Interestingly, long-range activated IrO_2 (rutile) has a similar activity to Ir black activated and Ir black long-range activated (Fig. 6) which might indicate some formation of hydrous oxides on IrO_2. Similarly, activated IrO_2 has similar OER activity to Ir black short-range activated. At this point, the question arises whether Raman spectroscopy will confirm these differences.

3.3. Ex situ Raman measurements

The spectra of drop-casted (as-deposited) GCE/IrO_2 and GCE/Ir black have already been discussed in *Section 3.1* (Fig. 4). In the following step, the *ex situ* Raman spectra were recorded for three different activated states and the degraded state (Table 5). The purpose of such different activations was to evaluate OER activities after them, and check whether any changes in the samples can be detected by Raman spectroscopy. The individual *ex situ* spectra that were measured at different locations are presented in Figs. S5 and S6 in *Supplementary information*, while their calculated average spectra are shown in Fig. 7. The spectra detected at different locations revealed that the samples did

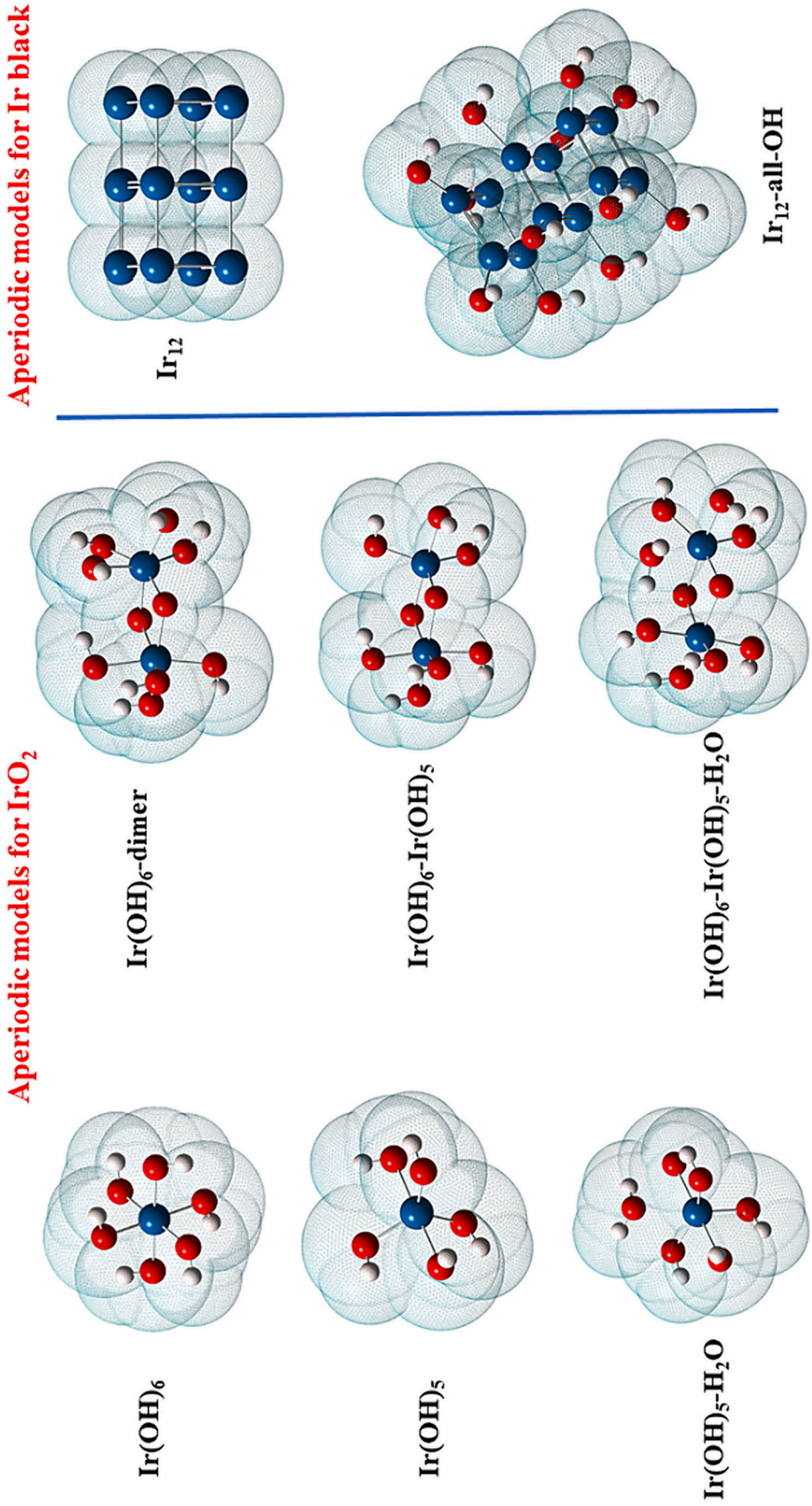

Fig. 5. Aperiodic models for the IrO_2 and Ir black.

Table 3
Comparison of the Raman signatures over various exchange-correlation functionals.

$Ir(OH)_5$ values are in (cm^{-1})	SDD-UB3LYP	SDD-UCAM-B3LYP	LANL2DZ-UCAM-B3LYP	LANL2DZ-UB3LYP
B_{1g}	142.32	156.19	146.40	140.85
E_g	554.60	586.32	582.84	550.44
B_{2g}	716.60	753.59	779.93	734.92
A_{1g}	744.06	781.23	803.89	763.75

In contrast to GCE/IrO_2, only two bands (552 cm^{-1} and 724 cm^{-1}) can be noted in the spectra of the as-deposited GCE/Ir black samples (Fig. 4B). More as-deposited spectra are shown in Fig. S6 A in *Supplementary information*. These are normalized to the 552 cm^{-1} band and differ slightly in the intensity of the broad band around 724 cm^{-1} (B_{2g} + A_{1g}). The spectra of the activated and long-range activated stats are very similar (Figs. S6 B,D), as are their average spectra in Fig. 7B. This correlates with the remarkably similar activity for OER observed in Fig. 6B, which could indicate alike active sites in both cases. However, it is interesting that the average spectrum of the activated-s.r. state stands out, probably due to a higher amount of oxide compared to the two other activation protocols. This is exactly the same state as stands out also in case of the GCE/IrO_2 samples (Fig. 7A).

Table 4
Raman shifts (in cm^{-1}) for aperiodic nanostructured oxides and incipient hydrous oxide with and without solvation effects.

Modes	$Ir(OH)_6$	$Ir(OH)_5$	$Ir(OH)_5$-H_2O	$Ir(OH)_6$-dimer	$Ir(OH)_6$- $Ir(OH)_5$	$Ir(OH)_6$- $Ir(OH)_5$-H_2O	Ir_{12}-all-OH	Ref. [29]
B_{1g}	218.10 (210.95)*	140.85 (134.95)	166.81 (139.89)	138.70 (134.86)	149.79 (165.53)	144.05 (148.69)	143.48 (142.89)	145
E_g	578.90 (565.25)	550.44 (551.99)	554.95 (542.28)	555.80 (541.05)	543.20 (546.70)	534.03 (545.35)	558.25 (532.74)	561
B_{2g}	627.70 (626.56)	734.92 (738.65)	726.16 (725.46)	738.05 (709.66)	720.11 (714.81)	729.25 (710.96)	707.48 (681.86)	728
A_{1g}	663.31 (662.08)	763.75 (754.84)	745.07 (742.15)	764.15 (756.49)	746.36 (727.02)	753.04 (757.44)	728.30 (749.25)	752

* Values in the brackets correspond to implicit solvation model.

not change in the same extent at each location, however, the individual spectra tend towards a certain average spectrum.

The measured GCE/IrO_2 spectra normalized to 557 cm^{-1} (E_g) band in Fig. S5 show the following features, as well as their average spectra in Fig. 7A:

- The as-deposited GCE/IrO_2 spectra (Fig. S5 A) predominantly show the more intense A_{1g} mode (746 cm^{-1}) with a B_{2g} shoulder (728 cm^{-1}), as already described in *Section 3.1*. (Fig. 4A).
- Short-range activation resulted in a considerable increase in the intensity of the B_{2g} band (shoulder) relative to the A_{1g} mode (Fig. S5 B). These spectra differ the most from the others.
- The activated spectra (Fig. S5 C) are the most similar to the as-deposited spectra (Figs. 4A, S5 A).
- The spectra of long-range activated and degraded states reveal similar features (Figs. S5 D,E). The B_{2g} and A_{1g} modes tend to merge into a broad band. The A_{1g} mode is slightly more intense in the spectra of activated-l.r. state.
- The same features are observed for the average spectra in Fig. 7A.

Table 5
The drop-casted samples prepared on GCE electrodes and conditions used for their activation and degradation.

Sample	State of the sample	Activation / degradation conditions
GCE	glassy carbon electrode	electrode surface
GCE/IrO_2	as-deposited	as-deposited (drop-casted)
	activated-short range (s.r.)	100 cycles, 300 mV/s, 1.1 to 1.6 V_{RHE}
	activated	100 cycles, 300 mV/s, 0.05 to 1.45 V_{RHE}
	activated-long range (l.r.)	100 cycles, 300 mV/s, 0.05 to 1.6 V_{RHE}
	degraded	activated, followed by 2 mA, 3600 rpm, 2 h
GCE/Ir black	as-deposited	as-deposited (drop-casted)
	activated-short range (s.r.)	100 cycles, 300 mV/s, 1.1 to 1.6 V_{RHE}
	activated	100 cycles, 300 mV/s, 0.05 to 1.45 V_{RHE}
	activated-long range (l.r.)	100 cycles, 300 mV/s, 0.05 to 1.6 V_{RHE}
	degraded	activated, followed by 2 mA, 3600 rpm, 2 h

GCE – glassy carbon electrode; s.r. – short range; l.r. – long range.

The characteristics of our measured *ex situ* spectra (Figs. 7, S5, S6) could not be directly correlated with the reported *in situ* ones [24,26,27] collected in Table 1. (i) First, the reported *in situ* Raman spectra were made on hydrous IrO_x films directly in electrolyte. By preparing electrodeposited IrO_x films, the authors avoided the adhesion problems of powdered drop-casted catalysts. (ii) Secondly, at applied potentials in electrolytes, these *in situ* studies report broad and partialy overlapping bands [24,26,27]. Similar broad bands were also noted in the first study of Pavlovic et al. [25], which was in their later work [26] designated as *ex situ*. It seems likely that the films were transferred under the Raman objective with the remaining electrolyte on its surface. Since our *ex situ* Raman spectra neither show any broad bands nor shifts of bands (Figs. 7, S5, S6), we assume that after rinsing with water, the samples did not show any solvation or adsorption effects, but mostly returned to the oxidation state of Ir^{4+}, a state similar to the as-deposited one. The exceptions are the IrO_2 and Ir black samples that were activated in the short range, *i.e.*, in the oxidation potential range (Figs. 7, S5, S6). Under such conditions, the B_{2g} band increases in intensity relative to A_{1g} band, which most probably indicates the tensions in the sample that is constantly exposed only to oxidation. For better insight, we intend to perform *in situ* measurements in the future. However, in the meantime, we decided to *mimick* an *in situ* experiment by measuring samples with the drop of electrolyte (Fig. 8).

During the *mimicked in situ* experiment, GCE/IrO_2 (Fig. 8A) and GCE/Ir black (Fig. 8B) samples were measured when soaked in the electrolyte (Figs. 8c) and activated (Figs. 8d). The transfer of the activated samples to the Raman spectrometer was made together with a drop of electrolyte. Activation was performed in the potential range 0.05 to 1.45 V_{RHE} with the ending potential being 0.05 V_{RHE}. This experiment revealed considerable differences between the both kinds of samples.

The bands at 557 (E_g) and, 728 (B_{2g}), 746 (A_{1g}) cm^{-1} dominated the initial spectrum of GCE/IrO_2 (Fig. 8A b). They can also be seen in the spectrum of the soaked sample as the crystalline structure does not change with soaking (Fig. 8A c). Any bands indicating hydration were not observed. However, after activation, two additional low-intensity bands could be seen at 465 and 634 cm^{-1} (Fig. 8A d) and, remain visible also when the electrolyte was poured off the sample (Fig. 8A e).

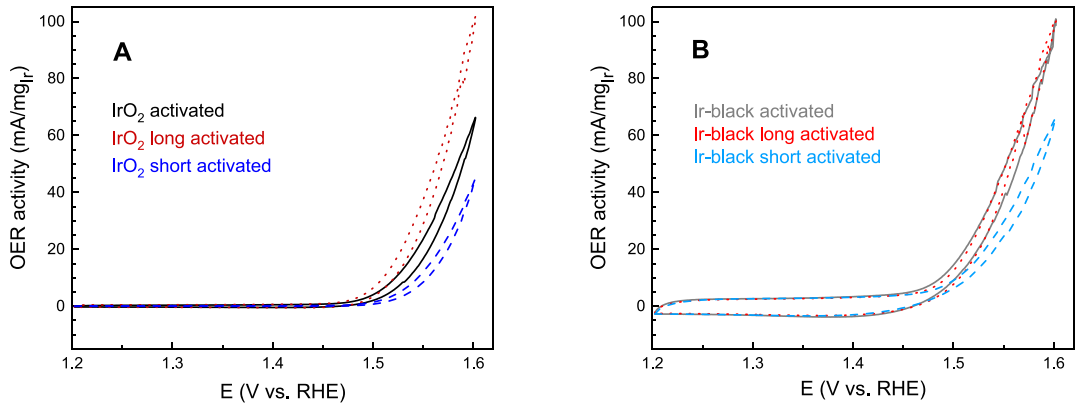

Fig. 6. OER activity after different activation protocols: A) GCE/IrO_2 (rutile) and B) GCE/Ir black.

Moreover, a detailed inspection of both spectra indicated that very low-intensity bands at 488 and 602 cm^{-1} could also be observed. After the sample was rinsed with MilliQ water (Fig. 8A f), intense bands that resembled the as-deposited ones re-appeared (Fig. 8A b). The question arose whether the 465 and 634 cm^{-1} bands are connected to adsorbed perchlorate ions or indicate the presence of Ir in 3+ state? Other candidates for Ir(3+) are low-intensity 488 and 602 cm^{-1} bands, which in spectra (Fig. 8A d,e) appear more like shoulders. The reasons for such questions are:

- In previous works of Raman spectroscopy of IrO_x films [25–27], the broad bands were marked as γ, δ, ε bands (Table 1) and ascribed to Ir—O stretching modes. The δ band at 602 cm^{-1} (at 0.8 V_{RHE} in 0.5 M H_2SO_4) [25] or 608 cm^{-1} (in 1 M $NaClO_4$ electrolyte) [27] was associated with the Ir(3+) centers.

- Formation of Ir^{3+} centers is expected when the electrochemical treatment is finished at 0.05 V_{RHE}. Moreover, IrO_x belongs to the electrochromic materials which are known to have a certain memory effect for reduced/oxidized states in air (during transfer!) when in the form of a covalently bonded film [66,67]. However, since our sample was a drop-casted suspension of IrO_2 on GCE, transferring the sample to Raman spectrometer (even under the drop of electrolyte) may affect its oxidation back to Ir^{4+}. It is also important to note that the current obtained during activation of rutile IrO_2 structure is low, which indicates that only small part of IrO_2 participates in redox reactions. This would support the very low-intensity Ir(3+) bands, as are those at 488 and 602 cm^{-1} in Fig. (8A d,e).

- The 0.1 M $HClO_4$ electrolyte has low-intensity bands around 465 and 634 cm^{-1}, while its most intense band appears at 936 cm^{-1}. Similarly, potassium perchlorate ($KClO_4$) has characteristic bands at 465, 630 and 943 cm^{-1} and, very low-intensity bands at 1089 and 1126 cm^{-1} [68]. These are exactly the bands that are present in the spectrum of the activated and dried states in Fig. 8A d,e. All these facts point to the conclusion that the 465 and 634 cm^{-1} bands could correspond to perchlorates that remained adsorbed to the dried sample.

On the contrary to the GCE/IrO_2 sample (Fig. 8A), the Raman spectrum of the GCE/Ir black in the activated state revealed broad spectral features (Fig. 8B c,d) that resemble the γ,δ and ε bands reported in the literature (Table 1) [24–27]. Unfortunately, the literature measurements were performed in different electrolytes and for electrodeposited hydrous IrO_x films, which resulted in somewhat different band positions (Table 1). In our activated GCE/Ir black spectrum, we observed a very broad band at 488 cm^{-1} with shoulders at 465, 602 and 634 cm^{-1}. The shape of this spectrum is similar to those obtained *in situ* in the region between Ir^{3+} and Ir^{4+} species in the work of Saeed et al. [27] who measured in 1 M $NaClO_4$ electrolyte. We can not compare our spectra to those reported in 0.5 M H_2SO_4 electrolyte since they do not cover the low potentials [24,26]. As well, the bands were not assigned to specific species, but only their overall shifts to the lower wavenumbers were ascribed to the reduction of Ir^{4+} to Ir^{3+} [24]. The intriguing feature is the Raman spectrum of the soaked sample (Fig. 8Bc), which shows similar characteristics as the spectrum after activation (Figure 8 Bd), only the intensity of the broad bands is much lower. This implies that solvation (hydration) also has a profound effect on the positions of bands, which has also been shown through DFT calculations (Table 4).

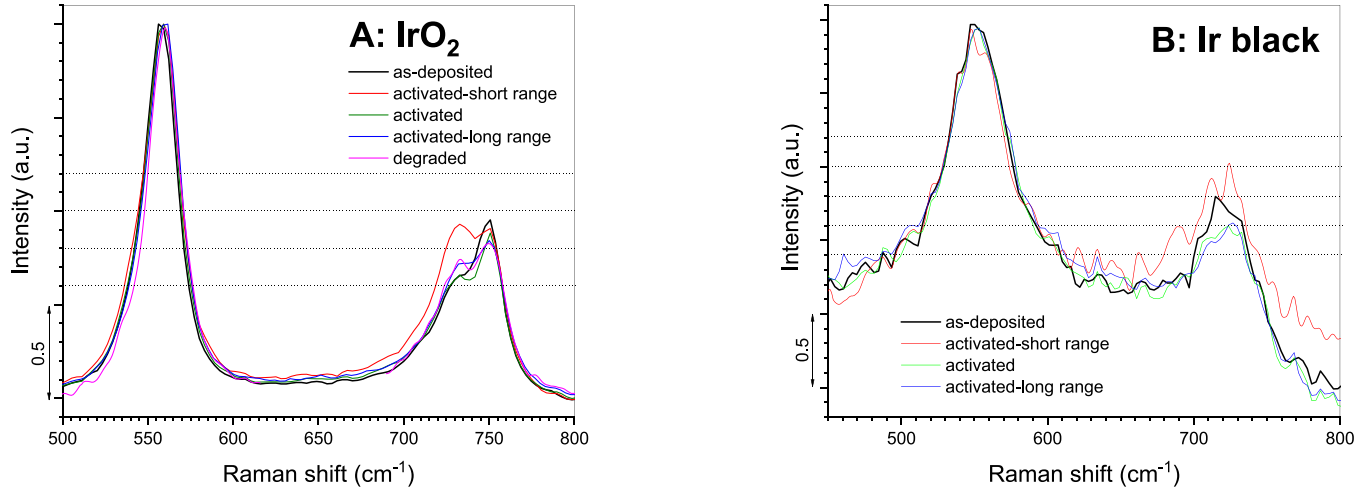

Fig. 7. Average *ex situ* Raman spectra of samples in as-deposited, activated-s.r., activated, activated-l.r. and degraded states: A) GCE/IrO_2 and B) GCE/Ir black. Average spectra were calculated from normalized spectra recorded at different locations on the sample. The power of the laser beam was 1.4 mW.

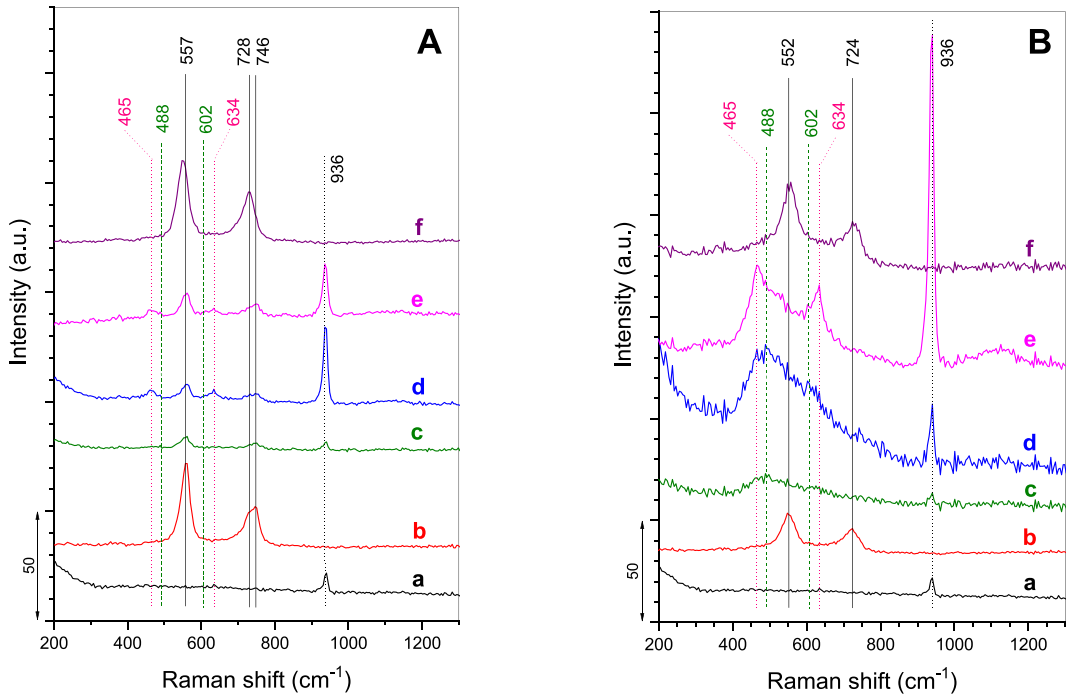

Fig. 8. Raman spectra of GCE/IrO_2 (A) and GCE/Ir black (B) in different states: b) as-deposited, c) soaked in the electrolyte, d) activated (the sample was kept under the drop of electrolyte), e) after activation when the drop of electrolyte was poured off and the sample was dried for 1 h, f) after activation, dried and finally rinsed with MilliQ water. Raman spectrum of 0.1 M $HClO_4$ electrolyte (a) is shown for comparison.

In the next step, when we poured off the electrolyte drop (0.1 M $HClO_4$) from our GCE/Ir black electrode and dried this sample in air for 1 h (Fig. 8B e), two distinct and intense bands at 465 and 634 cm^{-1} showed out. They are at the positions that imply the adsorbed perchlorates, which is also supported by the presence of a very intensive 936 cm^{-1} band and a broad band between 1050 and 1200 cm^{-1} [68]. The badly resolved shoulders are still visible at 488 and 602 cm^{-1}, the latter of which was - by using $H_2^{18}O$ and D_2O-based electrolytes - suggested to be associated with the Ir^{3+} [25–27]. When we rinsed our GCE/Ir black sample with water (Fig. 8B f), all the mentioned bands and shoulders moved to the positions as they were in the as-deposited sample (Fig. 8B b).

To obtain additional evidence of the oxidation states, XPS analysis of the Ir 4f region was performed (Fig. 9, Table 6), and peak fitting was conducted in the line with Refs. [33, 69]. Two characteristic sharp bands at 61.7 eV ($4f_{7/2}$) and 64.7 eV ($4f_{5/2}$) appeared in the spectrum of the rutile IrO_2 powder (Fig. 9A). Both values are in close agreement with those previously reported [9,33,69], confirming the presence of Ir in 4+ oxidation state. In contrast, XPS of Ir black powder revealed a broader envelope of peaks (Fig. 9B). The most intense peaks belong to metallic Ir^0 that appear at 60.9 eV ($4f_{7/2}$) and 63.9 eV ($4f_{5/2}$), *i.e.* in agreement with the reported values [69]. The area under the Ir^0 peaks (41.8%), however, is similar to the area under the Ir(4+) peaks (42%), suggesting that approximately equal amount of Ir is present in either 0 or 4+ states (Table 6). Ir in 4+ states was indirectly observed by EDS through the presence of oxygen (Table 2, Fig. 2, Fig. S1 in *Supplementary information*). Moreover, the characteristic E_g and $B_{2g} + A_{1g}$ bands of amorphous IrO_2 were also observed in the Raman spectra (Fig. 3). More unexpected is the presence of the 3+ oxidation state peaks at 62.4 eV ($4f_{7/2}$) and 65.3 eV ($4f_{5/2}$) in the XPS Ir 4f spectra (Fig. 9B), which indicate 16% of Ir (3+) in Ir black powder (Table 6). Literature search, however, revealed that a detailed analysis of XPS spectra was given for amorphous IrO_x, showing the presence of 20% of Ir(3+) in addition to 80% of Ir(4+) [69]. The percentage of Ir(4+) and Ir(3+) further increased to 43.7% and 20%, respectively, in the drop-casted GCE/Ir black sample in the as-deposited state (Fig. 9C, Table 6). This increase occurred at the expense of the decrease in the amount of the metallic Ir. After activation, a further increase in the amount of Ir(3+) was noted, as expected from the activation protocol.

XPS measurements (Fig. 9, Table 6) are in line with the *mimicked in situ* experiments (Fig. 8). The latter revealed bands related to perchlorate adsorption and Ir(3+)-O vibrations. XPS also suggested the presence of a small amount of Ir(3+) already in the as-deposited drop-casted GCE/Ir black sample (Fig. 9C). Together with the effect of hydration (Table 4), this would explain the similar shape of the soaked and activated Raman spectra of GCE/Ir black (Fig. 8B c,d). In addition, it would also explain the increase in the intensity of the shoulder band at 602 cm^{-1} that was in the previous works [25–27] associated with Ir(3+)-O vibrations, and eventually also the behavior of the band at 488 cm^{-1}. This band behaves similar to the 602 cm^{-1} band and may as well be connected with the Ir (3+)-O vibrations. The *mimicked in situ* Raman measurements also indicated the importance of the difference in the response of either firm rutile IrO_2 structure or Ir black nanoparticles to activation. The effect of solvation (hydration) on the band positions in the Raman spectra is also present. The intended *in situ* measurements, as well as the measurements in other type of acid electrolytes, are planned to get definitive answers on the influence of adsorption and hydration on the electrochemical processes of reduction, oxidation and OER activity of Ir-based samples. Moreover, future *in situ* measurements will provide valuable information on OER intermediates and active sites of electrocatalysts, as shown for other (Ni- and Co-based) electrocatalysts and other reactions [70–72]. Therefore, a possible difference of active sites due to different activation protocols could be highlighted in future *in situ* work. For this, the information gathered on perchlorate adsorption and Ir(3+)-O bands is precious for verifying the assignment of broad band features of *in situ* Raman measurements of various Ir-based samples [24,26,27].

4. Conclusions

Commercial Ir metal (Ir black) showed the presence of amorphous IrO_2 as evidenced by EDS analysis and Raman spectroscopy. Ir metal is Raman inactive, while rutile IrO_2 monocrystal has characteristic Raman

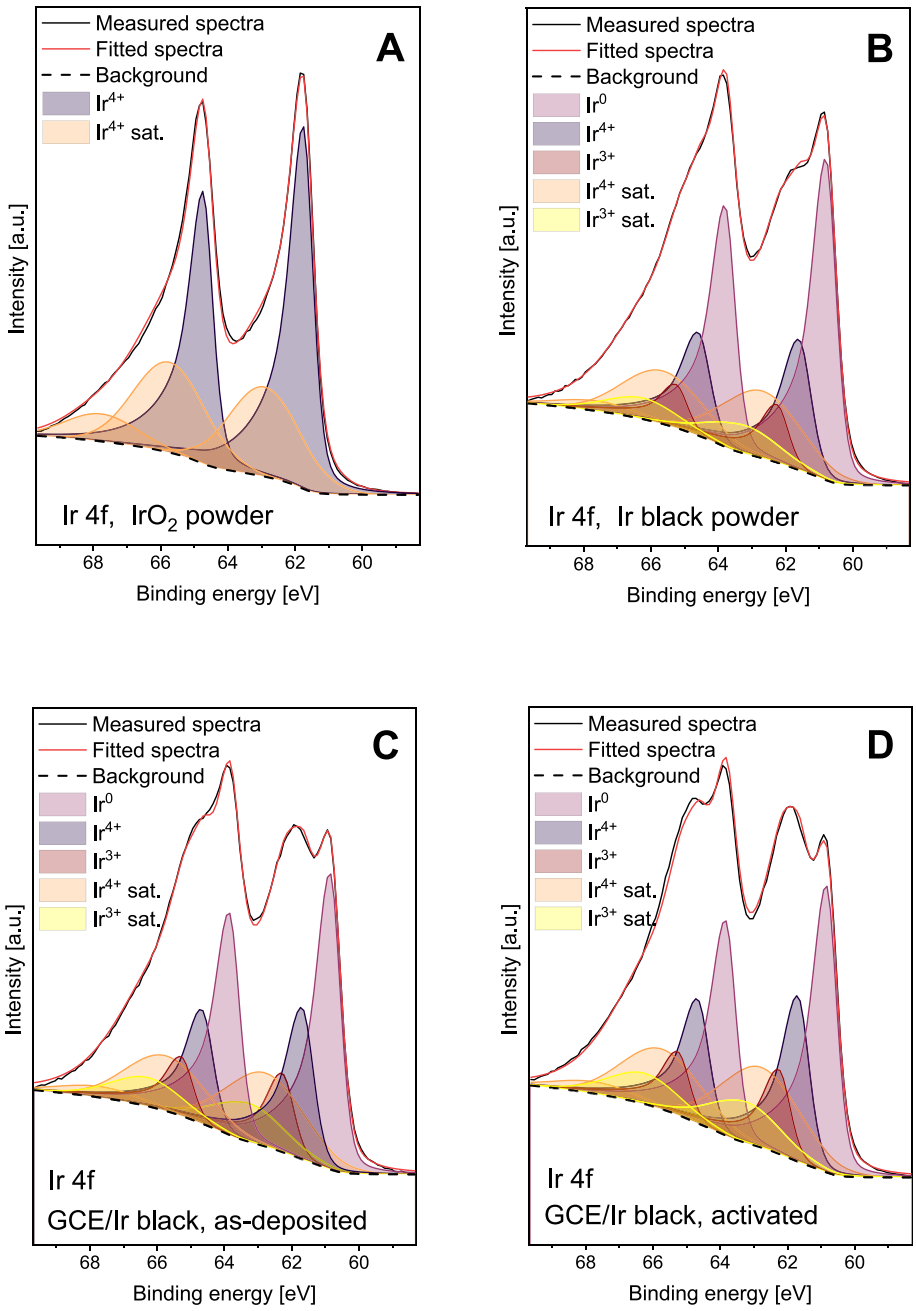

Fig. 9. XPS Ir 4f spectra of: A) IrO_2 powder, B) Ir black powder and C,D) drop-casted GCE/Ir black sample in as-deposited (C) and activated (D) states.

Table 6
Area (in %) under Ir 4f spectra of powders, and drop-casted GCE/Ir black sample in as-deposited and activated states.

Modes	IrO_2 powder	Ir black powder	GCE/Ir black as-deposited	GCE/Ir black activated[a]
Ir	0	41.8	36.3	33.8
Ir 4+	100	42.0	43.7	43.1
Ir 3+	0	16.2	20.0	23.2

[a] Activation was performed in the potential range 0.05 to 1.45 V_{RHE} according to Table 5.

modes at 752 (A_{1g}), 728 (B_{2g}) and 561 (E_g). In whis work, the IrO_2 and Ir black powders and drop-casted samples on GCE were screened using Raman spectroscopy to observe the possibilities of such measurements. It was interesting to notice that the positions of the Raman bands approached those of IrO_2 monocrystal when we switched from the powdered samples to samples drop-casted on GCE. This effect was more pronounced for IrO_2 than for Ir black, which can be ascribed to residual stress effects, particle size and microcrystallinity.

The electrochemical treatments of IrO_2 and Ir black (that were drop-casted on GCE) resulted in different OER activity. Namely, Ir black after activation and long-range activation, as well as IrO_2 long-range activated, presented the highest activity. On the other hand, IrO_2 short-range activated was the least active catalyst. This highlights the importance of activation protocols and their effect on the formed active sites for different catalysts. Furthermore, the Raman spectra of the electrocatalysts after different activations offer differences for the short range, hinting at a different chemical environment depending on the activation.

The drop-casted samples on GCE were first studied in an *ex situ* regime. The results showed that rinsing the samples with water before

Raman measurements caused their oxidation back to the 4+ state. The *mimicked in situ* measurements revealed formation of the broad bands for the GCE/Ir black sample (Fig. 8 Bd), while distinct bands were preserved for GCE/IrO_2 sample (Figure 8 Ad). Drying of both samples (Figs. 8A,B e) revealed new bands at 465 and 634 cm^{-1} that are tentatively ascribed to adsorbed perclorates. While these two modes appeared as distinct bands for the crystalline IrO_2 sample, they were accompanied by shoulder bands at 488 and 602 cm^{-1} for Ir black sample. The latter band corresponds to the position that was assigned to Ir(III) in the literature. DFT calcultations confirmed the importance of hydration (solvation) effects on the band positions.

CRediT authorship contribution statement

Leonard Moriau: Writing – original draft, Methodology, Investigation, Formal analysis, Data curation, Conceptualization. **Mohammed Azeezulla Nazrulla:** Writing – original draft, Software, Methodology, Data curation. **Anja Logar:** Methodology, Investigation, Formal analysis. **Luka Pavko:** Formal analysis. **Marjan Bele:** Methodology, Investigation, Formal analysis. **Nejc Hodnik:** Methodology, Funding acquisition, Conceptualization. **Angelja Kjara Surca:** Writing – original draft, Project administration, Methodology, Investigation, Funding acquisition, Formal analysis, Data curation, Conceptualization.

Declaration of competing interest

The authors declare that they have no known competing financial interests or personal relationships that could have appeared to influence the work reported in this paper.

Data availability

Data will be made available on request.

Acknowledgement

This work was supported by the Slovenian Research Agency through the funding of research program P2–0393 and projects J1–4401, N2–0155, N2–0248. M.A.N acknowledge the funding for Marie Skłodowska-Curie Actions, Individual Fellowships, project CO2-CAT-ALOG (grant reference no. 897866) from the EU commission for Horizon 2020 Framework Programme. The authors also acknowledge funding from the European Research Council (ERC) Starting Grant 123STABLE (Grant Agreement ID: 852208) and NATO Science for Peace and Security Program under Grant G5729.

Appendix A. Supplementary data

Supplementary data to this article can be found online at https://doi.org/10.1016/j.susmat.2024.e00901.

References

[1] Z.W. Seh, J. Kibsgaard, C.F. Dickens, I. Chorkendorff, J.K. Nørskov, T.F. Jaramillo, Combining theory and experiment in electrocatalysis: insights into materials design, Science (80) 355 (2017) 146, https://doi.org/10.1126/science.aad4998.
[2] V.R. Stamenkovic, D. Strmcnik, P.P. Lopes, N.M. Markovic, Energy and fuels from electrochemical interfaces, Nat. Mater. 16 (2016) 57–69, https://doi.org/10.1038/nmat4738.
[3] I. Katsounaros, S. Cherevko, A.R. Zeradjanin, K.J.J. Mayrhofer, Oxygen electrochemistry as a cornerstone for sustainable energy conversion, Angew. Chem. Int. Ed. 53 (2014) 102–121, https://doi.org/10.1002/anie.201306588.
[4] T. Reier, H.N. Nong, D. Teschner, R. Schlögl, P. Strasser, Electrocatalytic oxygen evolution reaction in acidic environments – reaction mechanisms and catalysts, Adv. Energy Mater. 7 (2017), https://doi.org/10.1002/aenm.201601275.
[5] T. Reier, M. Oezaslan, P. Strasser, Electrocatalytic oxygen evolution reaction (OER) on Ru, Ir, and pt catalysts: a comparative study of nanoparticles and bulk materials, ACS Catal. 2 (2012) 1765–1772, https://doi.org/10.1021/cs3003098.
[6] J. Ruiz Esquius, D.J. Morgan, I. Spanos, D.G. Hewes, S.J. Freakley, G.J. Hutchings, Effect of base on the facile hydrothermal preparation of highly active IrOx oxygen evolution catalysts, ACS Appl. Energy Mater. 3 (2020) 800–809, https://doi.org/10.1021/acsaem.9b01642.
[7] V.K. Puthiyapura, M. Mamlouk, S. Pasupathi, B.G. Pollet, K. Scott, Physical and electrochemical evaluation of ATO supported IrO2 catalyst for proton exchange membrane water electrolyser, J. Power Sources 269 (2014) 451–460, https://doi.org/10.1016/j.jpowsour.2014.06.078.
[8] D.H. Kim, S.H. Park, J. Choi, M.H. Yi, H.S. Kim, Fabrication of iridium oxide nanoparticles supported on activated carbon powder by flashlight irradiation for oxygen evolutions, Mater. Sci. Eng. B Solid-State Mater. Adv. Technol. 201 (2015) 29–34, https://doi.org/10.1016/j.mseb.2015.06.004.
[9] D.F. Abbott, D. Lebedev, K. Waltar, M. Povia, M. Nachtegaal, E. Fabbri, C. Copéret, T.J. Schmidt, Iridium oxide for the oxygen evolution reaction: correlation between particle size, morphology, and the surface hydroxo layer from operando XAS, Chem. Mater. 28 (2016) 6591–6604, https://doi.org/10.1021/acs.chemmater.6b02625.
[10] R. Badam, M. Hara, H.H. Huang, M. Yoshimura, Synthesis and electrochemical analysis of novel IrO2 nanoparticle catalysts supported on carbon nanotube for oxygen evolution reaction, Int. J. Hydrog. Energy 43 (2018) 18095–18104, https://doi.org/10.1016/j.ijhydene.2018.08.034.
[11] A. Lončar, D. Escalera-López, S. Cherevko, N. Hodnik, Inter-relationships between oxygen evolution and iridium dissolution mechanisms, Angew. Chem. Int. Ed. 61 (2022) e202114437, https://doi.org/10.1002/anie.202114437.
[12] J. Gao, C.Q. Xu, S.F. Hung, W. Liu, W. Cai, Z. Zeng, C. Jia, H.M. Chen, H. Xiao, J. Li, Y. Huang, B. Liu, Breaking long-range order in iridium oxide by alkali ion for efficient water oxidation, J. Am. Chem. Soc. 141 (2019) 3014–3023, https://doi.org/10.1021/jacs.8b11456.
[13] Y.M. Chen, C.A. Chen, Y.S. Huang, K.Y. Lee, K.K. Tiong, Synthesis of IrO2 nanocrystals on carbon nanotube bundle arrays and their field emission characteristics, J. Alloys Compd. 487 (2009) 659–664, https://doi.org/10.1016/j.jallcom.2009.07.181.
[14] R.S. Chen, Y.S. Huang, D.S. Tsai, S. Chattopadhyay, C.T. Wu, Z.H. Lan, K.H. Chen, Growth of well aligned IrO2 nanotubes on LiTaO3(012) substrate, Chem. Mater. 16 (2004) 2457–2462, https://doi.org/10.1021/cm030668n.
[15] L. Moriau, M. Bele, Ž. Marinko, F. Ruiz-Zepeda, G. Koderman Podboršek, M. Šala, A.K. Šurca, J. Kovač, I. Arčon, P. Jovanovič, N. Hodnik, L. Suhadolnik, Effect of the morphology of the high-surface-area support on the performance of the oxygen-evolution reaction for iridium nanoparticles, ACS Catal. 11 (2021) 670–681, https://doi.org/10.1021/acscatal.0c04741.
[16] M. Bele, K. Stojanovski, P. Jovanovič, L. Moriau, G. Koderman Podboršek, J. Moškon, P. Umek, M. Sluban, G. Dražič, N. Hodnik, M. Gaberšček, Towards stable and conductive titanium Oxynitride high-surface-area support for iridium nanoparticles as oxygen evolution reaction Electrocatalyst, ChemCatChem 11 (2019) 5038–5044, https://doi.org/10.1002/cctc.201901487.
[17] L. Moriau, G. Koderman Podboršek, A.K. Surca, S. Semsari Parpari, M. Šala, U. Petek, M. Bele, P. Jovanovič, B. Genorio, N. Hodnik, Enhancing iridium Nanoparticles' oxygen evolution reaction activity and stability by adjusting the coverage of titanium Oxynitride flakes on reduced graphene oxide Nanoribbons' support, Adv. Mater. Interfaces 8 (2021) 2100900, https://doi.org/10.1002/admi.202100900.
[18] G. Koderman Podboršek, A.R. Kamšek, A. Lončar, M. Bele, L. Suhadolnik, P. Jovanovič, N. Hodnik, Atomically-resolved structural changes of ceramic supported nanoparticulate oxygen evolution reaction Ir catalyst, Electrochim. Acta 426 (2022) 140800, https://doi.org/10.1016/j.electacta.2022.140800.
[19] L.J. Moriau, A. Hrnjić, A. Pavlišič, A.R. Kamšek, U. Petek, F. Ruiz-Zepeda, M. Šala, L. Pavko, V.S. Šelih, M. Bele, P. Jovanovič, M. Gatalo, N. Hodnik, Resolving the nanoparticles' structure-property relationships at the atomic level: a study of Pt-based electrocatalysts, IScience 24 (2021) 102102, https://doi.org/10.1016/j.isci.2021.102102.
[20] P. Jovanovič, N. Hodnik, F. Ruiz-Zepeda, I. Arčon, B. Jozinović, M. Zorko, M. Bele, M. Šala, V.S. Šelih, S. Hočevar, M. Gaberšček, Electrochemical dissolution of iridium and iridium oxide particles in acidic media: transmission Electron microscopy, electrochemical flow cell coupled to inductively coupled plasma mass spectrometry, and X-ray absorption spectroscopy study, J. Am. Chem. Soc. 139 (2017) 12837–12846, https://doi.org/10.1021/jacs.7b08071.
[21] O. Hollricher, Raman Instrumentation for Confocal Raman Microscopy, Springer S, Springer, Berlin, 2010.
[22] P.C. Liao, C.S. Chen, W.S. Ho, Y.S. Huang, K.K. Tiong, Characterization of IrO2 thin films by Raman spectroscopy, Thin Solid Films 301 (1997) 7–11, https://doi.org/10.1016/S0040-6090(96)09545-4.
[23] Z. Xu, Z. He, Y. Song, X. Fu, M. Rommel, X. Luo, A. Hartmaier, J. Zhang, F. Fang, Topic review: application of raman spectroscopy characterization in micro/nano-machining, Micromachines 9 (2018) 1–23, https://doi.org/10.3390/mi9070361.
[24] Y. Mo, I.C. Stefan, W. Bin Cai, J. Dong, P. Carey, D.A. Scherson, In situ iridium LIII-edge X-ray absorption and surface enhanced Raman spectroscopy of electrodeposited iridium oxide films in aqueous electrolytes, J. Phys. Chem. B 106 (2002) 3681–3686, https://doi.org/10.1021/jp014452p.
[25] Z. Pavlovic, C. Ranjan, Q. Gao, M. Van Gastel, R. Schlögl, Probing the structure of a water-oxidizing anodic iridium oxide catalyst using raman spectroscopy, ACS Catal. 6 (2016) 8098–8105, https://doi.org/10.1021/acscatal.6b02343.
[26] Z. Pavlovic, C. Ranjan, M. Van Gastel, R. Schlögl, The active site for the water oxidising anodic iridium oxide probed through: in situ Raman spectroscopy, Chem. Commun. 53 (2017) 12414–12417, https://doi.org/10.1039/c7cc05669a.
[27] K.H. Saeed, M. Forster, J.F. Li, L.J. Hardwick, A.J. Cowan, Water oxidation intermediates on iridium oxide electrodes probed by: in situ electrochemical SHINERS, Chem. Commun. 56 (2020) 1129–1132, https://doi.org/10.1039/c9cc08284k.

[28] C. Ma, W. Sun, W. Qamar Zaman, Z. Zhou, H. Zhang, Q. Shen, L. Cao, J. Yang, Lanthanides regulated the amorphization-crystallization of iro2for outstanding oer performance, ACS Appl. Mater. Interfaces 12 (2020) 34980–34989, https://doi.org/10.1021/acsami.0c08969.
[29] Y.S. Huang, S.S. Lin, C.R. Huang, M.C. Lee, Raman spectrum of IrO2, Solid State Commun. 70 (1989) 517–522, https://doi.org/10.1016/0038-1098(89)90942-3.
[30] S. Musić, S. Popović, M. Maljković, Ž. Skoko, K. Furić, A. Gajović, Thermochemical formation of IrO2 and Ir, Mater. Lett. 57 (2003) 4509–4514, https://doi.org/10.1016/S0167-577X(03)00352-5.
[31] P.C. Liao, Y.S. Huang, K.K. Tiong, Characterization of RuO2 and IrO2 films deposited on Si substrate, J. Alloys Compd. 317–318 (2001) 98–102, https://doi.org/10.1016/S0925-8388(00)01403-1.
[32] A.V. Korotcov, Y.S. Huang, D.S. Tsai, K.K. Tiong, Raman scattering characterization of vertical aligned 1D IrO2 nanocrystals grown on single crystal oxide substrates, Solid State Commun. 137 (2006) 310–314, https://doi.org/10.1016/j.ssc.2005.11.038.
[33] V. Pfeifer, T.E. Jones, J.J. Velasco Vélez, C. Massué, M.T. Greiner, R. Arrigo, D. Teschner, F. Girgsdies, M. Scherzer, J. Allan, M. Hashagen, G. Weinberg, S. Piccinin, M. Hävecker, A. Knop-Gericke, R. Schlögl, The electronic structure of iridium oxide electrodes active in water splitting, Phys. Chem. Chem. Phys. 18 (2016) 2292–2296, https://doi.org/10.1039/c5cp06997a.
[34] Y. Ping, G. Galli, W.A. Goddard, Electronic structure of IrO2: the role of the metal d orbitals, J. Phys. Chem. C 119 (2015) 11570–11577, https://doi.org/10.1021/acs.jpcc.5b00861.
[35] Y. Ping, R.J. Nielsen, W.A. Goddard, The reaction mechanism with free energy barriers at constant potentials for the oxygen evolution reaction at the IrO2 (110) surface, J. Am. Chem. Soc. 139 (2017) 149–155, https://doi.org/10.1021/jacs.6b07557.
[36] D.Y. Kuo, J.K. Kawasaki, J.N. Nelson, J. Kloppenburg, G. Hautier, K.M. Shen, D. G. Schlom, J. Suntivich, Influence of surface adsorption on the oxygen evolution reaction on IrO2(110), J. Am. Chem. Soc. 139 (2017) 3473–3479, https://doi.org/10.1021/jacs.6b11932.
[37] S. Czioska, A. Boubnov, D. Escalera-López, J. Geppert, A. Zagalskaya, P. Röse, E. Saraçi, V. Alexandrov, U. Krewer, S. Cherevko, J.D. Grunwaldt, Increased Ir-Ir interaction in iridium oxide during the oxygen evolution reaction at high potentials probed by operando spectroscopy, ACS Catal. 11 (2021) 10043–10057, https://doi.org/10.1021/acscatal.1c02074.
[38] S.M. Alia, G.C. Anderson, Iridium oxygen evolution activity and durability baselines in rotating disk electrode half-cells, J. Electrochem. Soc. 166 (2019) F282–F294, https://doi.org/10.1149/2.0731904jes.
[39] S. Gates-Rector, T. Blanton, The powder diffraction file: a quality materials characterization database, Powder Diffract. 34 (2019) 352–360, https://doi.org/10.1017/S0885715619000812.
[40] M.J. Frisch, G.W. Trucks, H.B. Schlegel, G.E. Scuseria, M.Y. Robb, J.R. Cheeseman, G. Scalmani, V. Barone, G.Y. Petersson, H. Nakatsuji, X. Li, M. Caricato, A. V. Marenich, J. Bloino, B.G. Janesko, R. Gomperts, B. Mennucci, H.P. Hratchian, J. V. Ortiz, A.F. Izmaylov, J.L. Sonnenberg, D. Williams-Young, F. Ding, F. Lipparini, F. Egidi, J. Goings, B. Peng, T. Petrone, A. Henderson, D. Ranasinghe, V. G. Zakrzewski, J. Gao, N. Rega, G. Zheng, W. Liang, M. Hada, M. Ehara, R. Toyota, K. Fukuda, J. Hasegawa, M. Ishida, T. Nakajima, Y. Honda, O. Kitao, H. Nakai, T. Vreven, K. Throssell, J.A. Montgomery, J.E. Peralta, F. Ogliaro, M.J. Bearpark, J. J. Heyd, E.N. Brothers, K.N. Kudin, V.N. Staroverov, T.A. Keith, R. Kobayashi, J. Normand, K. Raghavachari, A.P. Rendell, J.C. Burant, S.S. Iyengar, J. Tomasi, M. Cossi, J.M. Millam, M. Klene, C. Adamo, R. Cammi, J.W. Ochterski, R.L. Martin, K. Morokuma, O. Farkas, J.B. Foresman, D.J. Fox, Gaussian 16, Revision C.02, 2019.
[41] F. Glendening, E.D. Reed, A.E. Carpenter, J.E. Weinhold, NBO Version 3.1, 2003.
[42] K. Momma, F. Izumi, VESTA 3 for three-dimensional visualization of crystal, volumetric and morphology data, J. Appl. Crystallogr. 44 (2011) 1272–1276, https://doi.org/10.1107/S0021889811038970.
[43] S. Thanawala, D.G. Georgiev, R.J. Baird, G. Auner, Characterization of iridium oxide thin films deposited by pulsed-direct-current reactive sputtering, Thin Solid Films 515 (2007) 7059–7065, https://doi.org/10.1016/j.tsf.2007.02.090.
[44] D. González, M. Sodupe, L. Rodríguez-Santiago, X. Solans-Monfort, Surface morphology controls water dissociation on hydrated IrO2 nanoparticles, Nanoscale 13 (2021) 14480–14489, https://doi.org/10.1039/d1nr03592d.
[45] D. González, M. Sodupe, L. Rodríguez-Santiago, X. Solans-Monfort, Metal coordination determines the catalytic activity of IrO2 nanoparticles for the oxygen evolution reaction, J. Catal. 412 (2022) 78–86, https://doi.org/10.1016/j.jcat.2022.05.023.
[46] L. Ouattara, S. Fierro, O. Frey, M. Koudelka, C. Comninellis, Electrochemical comparison of IrO2 prepared by anodic oxidation of pure iridium and IrO2 prepared by thermal decomposition of H 2IrCl6 precursor solution, J. Appl. Electrochem. 39 (2009) 1361–1367, https://doi.org/10.1007/s10800-009-9809-2.
[47] S. Geiger, O. Kasian, B.R. Shrestha, A.M. Mingers, K.J.J. Mayrhofer, S. Cherevko, Activity and stability of electrochemically and thermally treated iridium for the oxygen evolution reaction, J. Electrochem. Soc. 163 (2016) F3132–F3138, https://doi.org/10.1149/2.0181611jes.
[48] S. Cherevko, T. Reier, A.R. Zeradjanin, Z. Pawolek, P. Strasser, K.J.J. Mayrhofer, Stability of nanostructured iridium oxide electrocatalysts during oxygen evolution reaction in acidic environment, Electrochem. Commun. 48 (2014) 81–85, https://doi.org/10.1016/j.elecom.2014.08.027.
[49] F. Bizzotto, J. Quinson, A. Zana, J.J.K. Kirkensgaard, A. Dworzak, M. Oezaslan, M. Arenz, Ir nanoparticles with ultrahigh dispersion as oxygen evolution reaction (OER) catalysts: synthesis and activity benchmarking, Catal. Sci. Technol. 9 (2019) 6345–6356, https://doi.org/10.1039/c9cy01728c.
[50] A. Loncar, L. Moriau, K. Stojanovski, F. Ruiz-Zepeda, P. Jovanovic, M. Bele, M. Gaberscek, N. Hodnik, Ir/TiONx/C high-performance oxygen evolution reaction nanocomposite electrocatalysts in acidic media: synthesis, characterization and electrochemical benchmarking protocol, J. Phys. Energy. 2 (2020) 02LT01, https://doi.org/10.1088/2515-7655/ab69a2.
[51] J. Augustynski, M. Koudelka, J. Sanchez, B.E. Conway, ESCA study of the state of iridium and oxygen in electrochemically and thermally formed iridium oxide films, J. Electroanal. Chem. 160 (1984) 233–248, https://doi.org/10.1016/S0022-0728(84)80128-X.
[52] H.N. Nong, H.S. Oh, T. Reier, E. Willinger, M.G. Willinger, V. Petkov, D. Teschner, P. Strasser, Oxide-supported IrNiOx core-shell particles as efficient, cost-effective, and stable catalysts for electrochemical water splitting, Angew. Chem. Int. Ed. 54 (2015) 2975–2979, https://doi.org/10.1002/anie.201411072.
[53] H.A. El-Sayed, A. Weiß, L.F. Olbrich, G.P. Putro, H.A. Gasteiger, OER catalyst stability investigation using RDE technique: a stability measure or an artifact? J. Electrochem. Soc. 166 (2019) F458–F464, https://doi.org/10.1149/2.0301908jes.
[54] Y.T. Kim, P.P. Lopes, S.A. Park, A.Y. Lee, J. Lim, H. Lee, S. Back, Y. Jung, N. Danilovic, V. Stamenkovic, J. Erlebacher, J. Snyder, N.M. Markovic, Balancing activity, stability and conductivity of nanoporous core-shell iridium/iridium oxide oxygen evolution catalysts, Nat. Commun. 8 (2017) 1–8, https://doi.org/10.1038/s41467-017-01734-7.
[55] J.A. Arminio-Ravelo, A.W. Jensen, K.D. Jensen, J. Quinson, M. Escudero-Escribano, Electrolyte effects on the electrocatalytic performance of iridium-based nanoparticles for oxygen evolution in rotating disc electrodes, ChemPhysChem 20 (2019) 2956–2963, https://doi.org/10.1002/cphc.201900902.
[56] K.A. Lewinski, D. van der Vliet, S.M. Luopa, NSTF advances for PEM electrolysis - The effect of alloying on activity of NSTF electrolyzer catalysts and performance of NSTF based PEM electrolyzers, ECS Meet. Abstr. MA2015–02 (2015), https://doi.org/10.1149/ma2015-02/37/1457, 1457–1457.
[57] A. Hartig-Weiss, M. Miller, H. Beyer, A. Schmitt, A. Siebel, A.T.S. Freiberg, H. A. Gasteiger, H.A. El-Sayed, Iridium oxide catalyst supported on antimony-doped tin oxide for high oxygen evolution reaction activity in acidic media, ACS Appl. Nano Mater. 3 (2020) 2185–2196, https://doi.org/10.1021/acsanm.9b02230.
[58] A. Lončar, D. Escalera-López, F. Ruiz-Zepeda, A. Hrnjić, M. Šala, P. Jovanovič, M. Bele, S. Cherevko, N. Hodnik, Sacrificial cu layer mediated the formation of an active and stable supported iridium oxygen evolution reaction electrocatalyst, ACS Catal. 11 (2021) 12510–12519, https://doi.org/10.1021/acscatal.1c02968.
[59] M. Scohy, C. Montella, F. Claudel, S. Abbou, L. Dubau, F. Maillard, E. Sibert, S. Sunde, Investigating the oxygen evolution reaction on Ir(111) electrode in acidic medium using conventional and dynamic electrochemical impedance spectroscopy, Electrochim. Acta 320 (2019) 134536, https://doi.org/10.1016/j.electacta.2019.07.047.
[60] S. Cherevko, S. Geiger, O. Kasian, A. Mingers, K.J.J. Mayrhofer, Oxygen evolution activity and stability of iridium in acidic media. Part 1. - Metallic iridium, J. Electroanal. Chem. 773 (2016) 69–78, https://doi.org/10.1016/j.jelechem.2016.04.033.
[61] S. Cherevko, S. Geiger, O. Kasian, A. Mingers, K.J.J. Mayrhofer, Oxygen evolution activity and stability of iridium in acidic media. Part 2. - Electrochemically grown hydrous iridium oxide, J. Electroanal. Chem. 774 (2016) 102–110, https://doi.org/10.1016/j.jelechem.2016.05.015.
[62] V.A. Saveleva, L. Wang, D. Teschner, T. Jones, A.S. Gago, K.A. Friedrich, S. Zafeiratos, R. Schlögl, E.R. Savinova, Operando evidence for a universal oxygen evolution mechanism on thermal and electrochemical iridium oxides, J. Phys. Chem. Lett. 9 (2018) 3154–3160, https://doi.org/10.1021/acs.jpclett.8b00810.
[63] K. Schweinar, B. Gault, I. Mouton, O. Kasian, Lattice oxygen exchange in rutile IrO2during the oxygen evolution reaction, J. Phys. Chem. Lett. 11 (2020) 5008–5014, https://doi.org/10.1021/acs.jpclett.0c01258.
[64] S.M. Alia, B. Rasimick, C. Ngo, K.C. Neyerlin, S.S. Kocha, S. Pylypenko, H. Xu, B. S. Pivovar, Activity and durability of iridium nanoparticles in the oxygen evolution reaction, J. Electrochem. Soc. 163 (2016) F3105–F3112, https://doi.org/10.1149/2.0151611jes.
[65] E. Oakton, D. Lebedev, M. Povia, D.F. Abbott, E. Fabbri, A. Fedorov, M. Nachtegaal, C. Copéret, T.J. Schmidt, IrO2-TiO2: a high-surface-area, active, and stable electrocatalyst for the oxygen evolution reaction, ACS Catal. 7 (2017) 2346–2352, https://doi.org/10.1021/acscatal.6b03246.
[66] C.G. Granqvist, Handbook of Inorganic Electrochromic Materials, Amsterdam, 1995.
[67] A.K. Surca, G. Dražić, M. Mihelčič, Low-temperature V-oxide film for a flexible electrochromic device: comparison of its electrochromic, IR and Raman properties to those of a crystalline V <inf>2</inf> O <inf>5</inf> film, Sol. Energy Mater. Sol. Cells 196 (2019) 185–199, https://doi.org/10.1016/j.solmat.2019.03.017.
[68] F. Zapata, C. García-Ruiz, The discrimination of 72 nitrate, chlorate and perchlorate salts using IR and Raman spectroscopy, Spectrochim. Acta - Part A Mol. Biomol. Spectrosc. 189 (2018) 535–542, https://doi.org/10.1016/j.saa.2017.08.058.
[69] V. Pfeifer, T.E. Jones, J.J. Velasco Vélez, C. Massué, R. Arrigo, D. Teschner, F. Girgsdies, M. Scherzer, M.T. Greiner, J. Allan, M. Hashagen, G. Weinberg, S. Piccinin, M. Hävecker, A. Knop-Gericke, R. Schlögl, The electronic structure of iridium and its oxides, Surf. Interface Anal. 48 (2016) 261–273, https://doi.org/10.1002/sia.5895.

[70] M. Chen, D. Liu, L. Qiao, P. Zhou, J. Feng, K.W. Ng, Q. Liu, S. Wang, H. Pan, In-situ/operando Raman techniques for in-depth understanding on electrocatalysis, Chem. Eng. J. 461 (2023) 141939, https://doi.org/10.1016/j.cej.2023.141939.
[71] F. Luo, S. Pan, Y. Xie, C. Li, Y. Yu, H. Bao, Z. Yang, Hydrazine-assisted acidic water splitting driven by iridium single atoms, Adv. Sci. 10 (2023) 2305058, https://doi.org/10.1002/advs.202305058.
[72] F. Luo, S. Pan, Y. Xie, C. Li, Y. Yu, Z. Yang, Atomically dispersed Ni electrocatalyst for superior urea-assisted water splitting, J. Energy Chem. 90 (2024) 1–6, https://doi.org/10.1016/j.jechem.2023.10.007.